



# Simplify your imaging workflows

**Make research imaging workflows accessible, traceable,  
and secure with Athena Software for Core Imaging Facilities.**

Thermo Scientific™ Athena Software is a premium imaging data management platform designed for core imaging facilities that support materials science research.

Athena Software ensures traceability of images, metadata, and experimental workflows through an intuitive and collaborative web interface.

Find out more at [thermofisher.com/athena](https://thermofisher.com/athena)

**ThermoFisher**  
SCIENTIFIC

# Near-Infrared Light Triggered Self-Powered Mechano-Optical Communication System using Wearable Photodetector Textile

Linlin Li, Depeng Wang, Dong Zhang, Wenhao Ran, Yongxu Yan, Zhixin Li, Lili Wang,\* and Guozhen Shen\*

The merging of humans and machines depends on the contact sensor medium used. However, this contact interaction inevitably leads to mechanical loss. Photodetectors are cutting-edge tools in optical communication that use controlled lighting to achieve efficient signal conversion to drive mechano-optical communication systems and provide an innovative interface for the Internet of Things services. Here, a self-powered, non-contact mechano-optical communication system based on a wearable Te@TeSe photodetector textile is presented, which encodes near-infrared light to modulate robotic manipulator actions. The wearable Te@TeSe photodetector textile enhanced the photocurrent and responsivity by 400 times compared to a pristine Te nanowire (NW) array. The type II heterojunction of Te@TeSe NWs is proved by first-principles calculations and simulated, providing insights on photogenic carrier transmission in Te@TeSe NWs. This system shows the possibility of duplicate real-time execution of mechanical gestures in virtual environments and paves the way for advanced optical devices applied to information transmission and mechano-optical communication.

However, traditional contact sensing and manipulation methods cannot meet these requirements owing to mechanical fatigue and wear and tear. In addition, driving these sensors cannot work without electric power, which is not satisfactory in a limited energy supply situation.<sup>[4]</sup> Therefore, it is of great significance to develop a self-powered, noncontact sensor that can directly and seamlessly combine with an interactive interface to realize a universal and arbitrary communication system. The sensor helps the soft robot to perceive and interact with the environment through self-generated or transformed signals, which is a highly compatible scheme with a soft robot. Recently, various methods for soft robot sensing were reported, such as light detection, triboelectricity, piezoelectricity, electromagnetic effect, and conductive nanocomposites. Among the different interactive strategies, optical communica-

## 1. Introduction


With the emergence of artificial intelligence and the Internet of Things (IoT) demand for improved smart sensors for human-machine interaction (HMI) has not only increased but changed communication between people and the environment.<sup>[1,2]</sup> Currently, the control operation of various electrical equipment and systems, from household appliances to hospital patients' wheelchairs or roadside lamp switches, is achieved by using external-physical-force-driven and self-propelled mechanisms.<sup>[3,4]</sup>

tions typically enable long-range, dexterous, precise, fast, and robust actuation and control of robotic manipulators.<sup>[5]</sup> Photodetectors are important for optical communication applications and are key components of mechano-optical communication systems that use controlled lighting to achieve efficient signal conversion to drive robotic manipulator actions.<sup>[6–8]</sup> In having good flexibility and a high response, the speed photodetector can accurately and quickly identify the optical signal and drive the soft robotic manipulator. Additionally, the rapid development of material science and processing technology has made multifunctional flexible and wearable devices possible.<sup>[9]</sup> Among them, fiber-shaped photodetectors have proven to be smart platforms for building wearable optical communication systems. However, unlike fiber-shaped energy storage units which are easy to weave into devices, the fiber-shaped photodetectors reported at present are mainly made of bulky metal wires-based inorganic semiconductors, which have poor flexibility.<sup>[9]</sup> The optical fiber photodetector constructed by direct braiding inevitably destroys its surface structure, resulting in performance degradation of low responsivity and switching ratio. A good method is to make photodetectors directly on the pre-braided fabric to avoid surface damage to the fiber photodetector during the braiding process.

Here, we propose the direct growth of Te@TeSe nanowires (NWs) on carbon fiber fabric (CFF) to fabricate wearable

L. L. Li, D. P. Wang, Dr. D. Zhang, W. H. Ran, Y. X. Yan, Z. X. Li, Prof. L. L. Wang, Prof. G. Z. Shen  
State Key Laboratory for Superlattices and Microstructures  
Institute of Semiconductors  
Chinese Academy of Sciences  
Beijing 100083, China  
E-mail: liliwang@semi.ac.cn; gzshen@semi.ac.cn

L. L. Li, D. P. Wang, Dr. D. Zhang, W. H. Ran, Y. X. Yan, Z. X. Li, Prof. G. Z. Shen  
Center of Materials Science and Optoelectronic Engineering  
University of Chinese Academy of Sciences  
Beijing 100029, China

 The ORCID identification number(s) for the author(s) of this article can be found under <https://doi.org/10.1002/adfm.202104782>.

DOI: 10.1002/adfm.202104782



photodetector textiles and apply them to a mechanical–optical communication system. Its functions can modulate robotic manipulators remotely, accurately, and quickly by using external near-infrared (NIR) light. Systematic investigations on the photoresponse characteristics of individual Te@TeSe NW array photodetectors have implied their ultrahigh light dark current ratio, high response speed, and excellent stability. The type II heterojunction of Te@TeSe NWs was proved by first-principles calculations and simulated, providing insights on photogenic carrier transmission in Te@TeSe NWs. In addition, NIR controls the motion of the robot hand via a photodetector as a proof of concept for human–computer interaction. This research is an important attempt to realize advanced electronic devices applied to information transmission and human–computer interaction.

## 2. Results and Discussion

### 2.1. Mechanical–Optical Communication Platform

Compared with the traditional HMI system,<sup>[10–12]</sup> the proposed mechanical–optical communication system could utilize the

CFF conductive textile photodetector coated with the Te@TeSe nanowires serving as the core of optical communication to convert external NIR signals into electrical signals, drive the optical-machine communication by self-power, then use encoded NIR to send specific instructions to the processing circuit and modulate the soft robotic manipulators (e.g., reach, grasp, and carry in **Figure 1a**). **Figure 1b** shows the photodetector's structure, Te@TeSe NW arrays were quasi-vertically grown on the CFF textile, where all the Te@TeSe nanowires were 100 nm wide (**Figure S1**, Supporting Information). Moreover, a polymethyl methacrylate (PMMA) layer was spanned on the nanowire arrays to prevent short circuits from isolating the top and bottom electrodes and for protecting the nanowire arrays (**Figure S2**, Supporting Information). Finally, an Ag NW layer was assembled on the functional textile as the top electrode by spin-coating to finish the fabrication of the wearable photodetector textile (**Figure S2**, Supporting Information). **Figure S3**, Supporting Information, shows the detailed fabrication methods of the photodetectors in the Experimental Section. The various encoded signals were recognized by the photodetector when NIR was encoded, resulting in signal conversion to drive robotic manipulator actions. This high

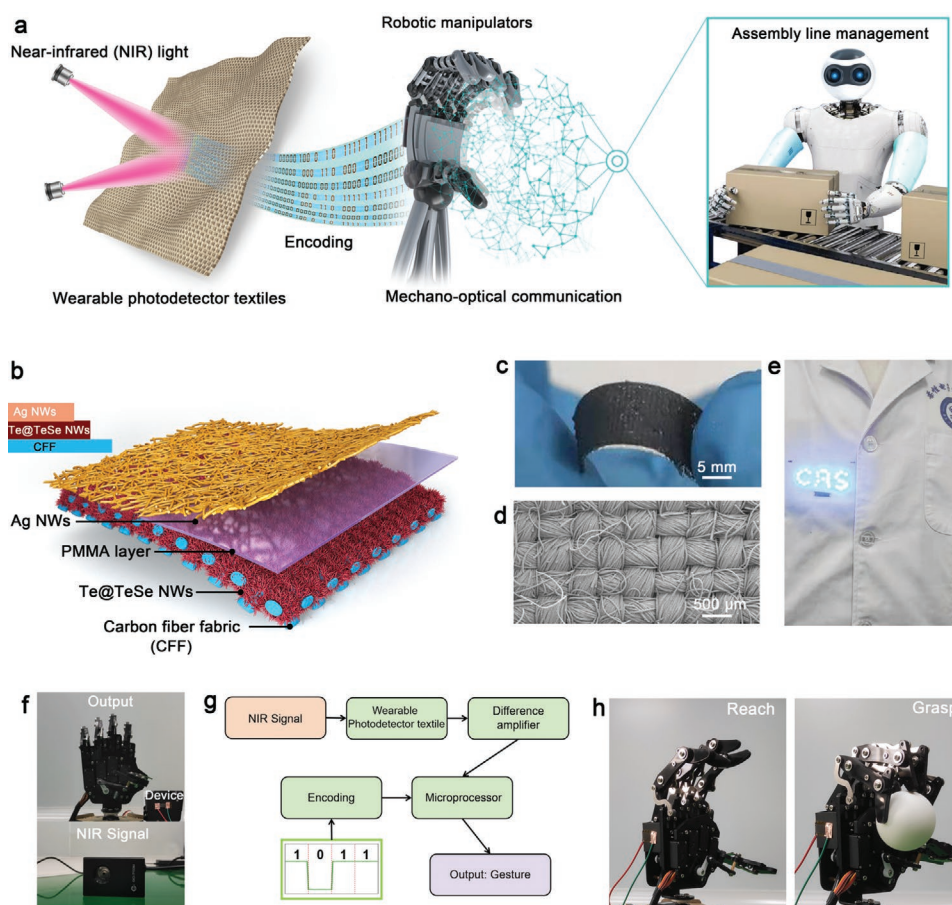


**Figure 1.** Mechanical–optical communication platform. a) Flexible photodetector covert NIR light to electrical signals to drive the soft robotic manipulators and the proposing applications of light-machine interface platform. This process will support the evolution from touch to light-operated electronics system. b) Schematic illustration and c) optical image of wearable photodetector. d) Top-view SEM image of Te@TeSe-CCF textile assembled with the Ag NWs. e) Optical image of wearable photodetector textile on clothes. f–h) Demonstration of the light-machine interface system based on the textiles to control robotic manipulators actions.

response ability enabled the mechanical movement to be consistent and avoided the deviation caused by uncontrollable touch.

Benefiting from the soft, flexible, and thin features of this photodetector textile, the photodetector could be woven into a piece of fabric evenly with human clothes and is compatible with various types of soft robots, including rigid materials. Here, we successfully demonstrated that the photoelectric detector and soft manipulator were assembled into an optical mechanical interaction system to realize manipulator operation. Figure 1f–g shows a system-level overview of the mechanical–optical communication platform. The photodetector textile effectively identified the NIR signal to achieve signal conversion, and generate output potential signals, which are amplified by a difference amplifier, and then converted into a digital signal through the analog-to-digital interface in the microprocessor. Subsequently, the microprocessor recognized these digital signals and transmitted the processed results to soft robotic manipulators for operation in a virtual environment (such as reach and grasp in Figure 1h). Figure 1a illustrates the proposed optical-machine communication system's displayed potential in the intelligent assembly lines, smart factories, unmanned warehouses, and IoT fields.

## 2.2. Material Characterization and Properties

Further improvement of the photoresponse resolution could be accomplished by rational design of Te@TeSe NWs. **Figure 2a** shows an illustration of the atomic structure of Te. A single-crystal Te was composed of ternary helical chains of Te atoms, and the helical chains were bound to a hexagonal system by van der Waals forces.<sup>[13]</sup> In this structure, only the two closest Te atoms in the spiral chain, which were stacked by van der Waals forces, formed a chemical bond. Therefore, Te prefers to grow along the [001] direction, which meant that it was easy to obtain Te NW, and the homogeneous and well-oriented Te nanowire arrays could be obtained experimentally. Se, a homologous and adjacent element of Te, had the same outer electronic structure and similar chemical and physical properties.<sup>[14]</sup> When Te and Se formed an alloy with an atomic number ratio of 1:1, the lattice structure of the alloy was similar to that of the Te crystal (see Figure 2b). When viewed from the *c*-axis, TeSe maintains a triangular spiral chain structure (towards the top of Figure 2b). The zigzag layers were stacked together via van der Waals forces in the view of the *a*-axis (middle of Figure 2b).<sup>[15,16]</sup> The proportion of atoms in the single chain was 1:1, which could be regarded as Se replacing half of the atoms in the Te nanowires.

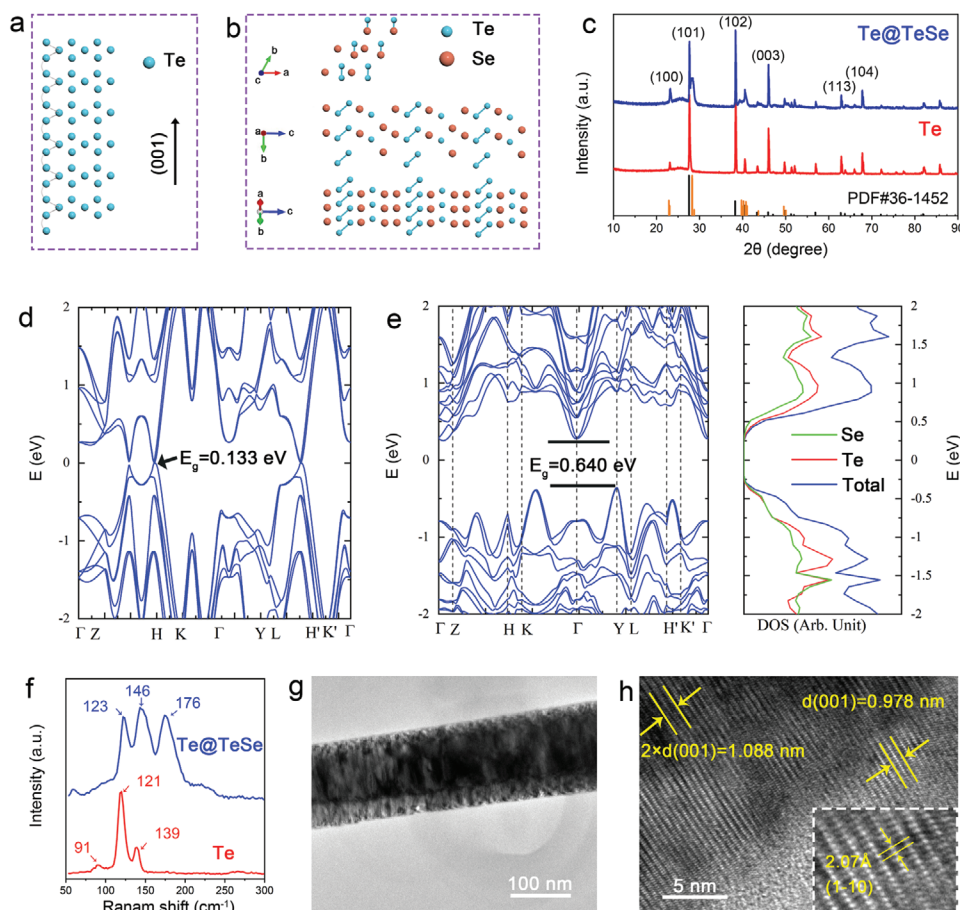


**Figure 2.** Te@TeSe NWs material characterization. a) Schematic diagram of Te atomic structure. b) Atomic structure of TeSe in different view: [001]; [100]; [110]. c) The X-ray diffraction (XRD) patterns of Te and Te@TeSe nanowire arrays. d) Band structure of Te. e) Band structure and density of states of TeSe alloy. f) Raman spectrum of Te and Te@TeSe nanowire arrays. g) The TEM images of Te@TeSe nanowire. h) The HRTEM of Te@TeSe nanowire.

To confirm that Te nanowire is single-crystalline and there is TeSe film covered on the Te nanowire array, several characterization analyses concluding XRD, transmission electron microscopy (TEM), and Raman scatter was conducted. Figure 2c illustrates the XRD patterns of Te and Te@TeSe nanowire arrays. The XRD peaks of Te nanowire arrays match well with the PDF#36-1452, which further confirms the successful preparation of Te nanowire arrays. The blue line in Figure 2c shows the XRD pattern of Te@TeSe, in which the XRD peaks of Te could be easily identified. Ignoring the XRD peaks of Te nanowires, there are three relatively obvious peaks, which are roughly located at 23°, 28°, and 40° respectively. The strongest of three XRD peaks includes the diffraction peaks of TeSe (10 $\bar{2}$ ), (112), and (01 $\bar{2}$ ) planes. The diffraction peaks of TeSe (100) and (010) planes show together as the second peak of intensity. The three XRD peaks match well with the simulated results. The XRD analysis confirms nanowire made up of Te and TeSe. Considering the experimental process, it can be roughly confirmed TeSe film covered on the Te nanowire array. The construction of heterojunction can effectively regulate photogenic carrier transmission in Te@TeSe NWs. In pristine Te NWs, the photo-generated carriers are easy to recombine with each other in the long migration process, and it is difficult to form obvious electrical signal output. When Te and TeSe are in contact, electrons on the contact surface transfer to TeSe and holes transfer to Te due to the work functions of Te and TeSe are 4.19 and 4.26 eV, respectively, as shown by our first-principles calculations (see Experimental Section for computation details, Figure 2d–e). Raman scatter further confirms nanowire made up of Te and TeSe (Figure 2f). The Raman spectrum of Te nanowire arrays gives three vibrational modes at 92, 121, and 140 cm<sup>-1</sup> corresponding to the E1-TO, A, and E2 peaks, which are almost consistent with previous literature reports.<sup>[17]</sup> Regardless of the Raman scattering peak of Te, the remaining part is the same as that of Te<sub>0.5</sub>Se<sub>0.5</sub> in previous literature reports, which can be seen clearly in Figure S4, Supporting Information. There are two main vibrational modes at 143 and 174 cm<sup>-1</sup>.<sup>[18–20]</sup>

Figure 2g shows the TEM image of a typical Te@TeSe nanowire with a diameter of ≈100 nm. The corresponding High-resolution TEM (HR-TEM) image displays the continuous crystal lattice of the Te@TeSe (Figure 2h and Figure S5a, Supporting Information). The left-up measured lattice constant is ≈0.544 nm, which is assignable to the (001) plane of the Te crystal (Figure S6, Supporting Information). The right-up measured lattice constant is ≈0.978 nm, which is assignable to the (001) plane of the TeSe crystal and the right-bottom measured lattice constant is ≈0.207 nm, which is assignable to the (1 $\bar{1}$ 0) plane of the TeSe crystal. Along the <001> direction, atomic layer interval of Te crystal is ≈0.181 nm, slightly larger than that of TeSe crystal, 0.163 nm. The lattice mismatch is ≈9.9%. Some slight lattice distortion can be observed near the Te lattice. Because of the two crystal stacked via van der Waals force, the compressive stress in Te lattice caused by the lattices mismatch is light. But, the light compressive stress impacts the vibrational mode of Te atom, which could cause the blue-shift of the Raman peaks at 121 and 139 cm<sup>-1</sup>, as Figure 2f. The corresponding selected area electron diffraction (SAED) pattern of the TeSe shows bright diffraction spots with a rectangular shape (Figure S5b, Supporting Information). The spot away

from the diffraction center divides into two spots; that indicates there are two crystals in this region that are structurally similar with different lattice constants, which are Te and TeSe. Both the HR-TEM and selected area electron diffraction (SAED) confirm that Te nanowire is single-crystalline and there is TeSe film covered on the Te nanowire array. The X-ray energy dispersive spectrum (EDS) visually illustrates the Te and Se element distribution in nanowires (Figure S7, Supporting Information), the density of Te in the middle is greater than that on both sides, which is typical nanowire strength distribution, and Se distributed with the same area size (Figure S8, Supporting Information). The distribution of Te and Se further demonstrates that the TeSe alloy is covered on Te nanowire arrays. Through the analyses above, we confirmed the successful preparation of Te nanowire arrays and Te@TeSe nanowire arrays.

### 2.3. Photodetector Device Characteristics and Theoretical Analyses

Figure 3a shows the *I*–*V* curves of the Te and Te@TeSe nanowire array photodetector irradiated by 1550 nm light or under dark conditions. There was a distinct light response of the Te@TeSe NW array photodetector when 1550 nm light was turned on, but the *I*–*V* curves of the Te NW array photodetector irradiated by 1550 nm light and under dark conditions were almost identical, which confirmed that coating TeSe on Te NWs could significantly improve its photoresponse at 1550 nm. On/off ratio is an important figures-of-merit defining the performance of photodetectors, which can be calculated as  $I_{\text{(on/off)}} = (I_{\text{light}} - I_{\text{dark}})/I_{\text{dark}} = \Delta I/I_0$ .<sup>[21,22]</sup> Then, the  $\Delta I/I_0$  of the Te@TeSe nanowire arrays photodetector is about 400 times higher than pristine Te nanowire arrays photodetector at 1550 nm. The difference in the performance of the photodetectors is shown via the time-dependent response of the two photodetectors at zero bias under 1550 nm light (Figure 3b). The  $\Delta I/I_0$  of the Te@TeSe nanowire array photodetector was 85, much larger than that of the Te nanowire array photodetector, which was 0.2 (magnified 100 times in Figure 3b). In addition, the performance enhancement can be viewed at all other wavelengths used, 915, 1064, 1122, 1342, 1450, and 1550 nm (Figure S9, Supporting Information). The comparison of two devices illuminated by 915 to 1550 nm light confirms that coating TeSe on Te NWs can significantly enhance photodetector performance.

Therefore, covering TeSe on Te NWs could significantly improve the photodetector performance. The mechanism was investigated, and it could be explained as the follows (Figure 3c,d). In pristine Te NWs, the photo-generated carriers could easily recombine with each other during the long migration process, and it was difficult to form an obvious electrical signal output. Therefore, we attempted to construct a heterojunction to solve this problem. Based on the information obtained from the XRD pattern, the band structures and density of states (DOS) of Te and TeSe are calculated by the first-principles calculations (Figure 2d,e). The pristine Te crystal possesses a direct band gap about 0.133 eV locating at the H and H' valleys, while the TeSe compound is a semiconductor with an indirect band gap about 0.640 eV, the minimum of the



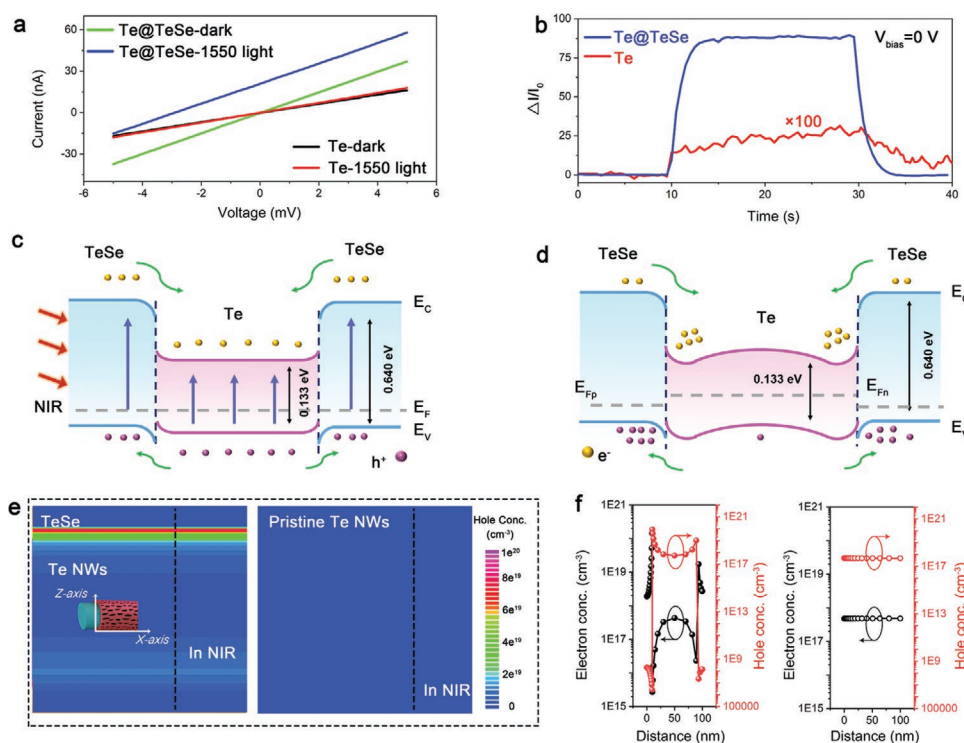


**Figure 3.** The simulated carrier concentration and corresponding tested photocurrent in devices. a)  $I$ - $V$  curves of the Te and Te@TeSe photodetector illuminated by 1550 nm light, and in dark. b) Time-dependent response of the Te and Te@TeSe photodetector at zero bias under 1550 nm light. Energy band diagram c) before and d) after charge transfer to explain performance enhancement mechanism. e) Simulated distributions of hole concentration in the Te@TeSe NWs and pristine Te NWs device in NIR, respectively. The inset in (e) is the model schematic illustration of the Te@TeSe NWs. f) Simulated distributions of electron and hole concentration in the cross sections along the dashed black lines in (e) for the Te@TeSe NWs and pristine Te NWs device.

conduction band occurs at the Gamma point and the maximum of the valence band occurs at the Y point. The DOS of TeSe show almost equivalent components for Te atoms and Se atoms in the vicinity of the Fermi level, as a natural reflection of the equal components of both elements in the compound formula. The chemical potentials for Te and TeSe are computed by construction of ultrathin slabs, respectively. Therefore, an internal electric field was formed at the interface in the direction from Te to TeSe, and a type II heterojunction was formed (Figure 3c). When the Te@TeSe NW was illuminated, the photogenerated carriers in the depletion region were affected by the internal electric field, and the photogenerated electrons were transferred to Te, while the photogenerated holes were transferred to TeSe, which reduced the probability of recombination between the carrier and prolongs the carrier life (Figure 3d). From the perspective of the carrier migration process, the Te on the surface of the Te@TeSe NWs forms a hole transport layer, and the TeSe in the core forms the electron transport layer. The migration of holes and electrons in the same medium was avoided, the probability of recombination was reduced, and the carrier life was prolonged in Te@TeSe NWs compared with pure Te NWs. Overall, the band structure and carrier distribution of Te@TeSe revealed the mechanism accounting for the much higher performance of the Te@TeSe NWs than that of the pristine Te NWs.

Further, we used Silvaco to verify the photoelectric mechanism of the heterostructure.<sup>[23]</sup> When irradiated by NIR light, the holes in the composite were unevenly distributed and the

hole concentration was much higher than that in the pristine Te NWs (Figure 3e,f). Because Te NWs and TeSe were both p-type semiconductors, there was a high hole concentration in Te NWs under NIR light, while the hole concentration in the TeSe shell was much lower than the electron concentration, which proved that the type-II heterojunction between Te and TeSe could drive the migration of photogenerated electrons from Te NWs to the TeSe shell, leaving holes behind.<sup>[24–26]</sup> In addition, the electron and hole distributions in Te@TeSe were uneven, and the hole concentration near the Te and TeSe interface was higher than that in the Te center, while the hole concentration distribution was opposite, which proved that traps in TeSe could produce a local positive gating effect. When the device was in the dark, the charge and hole distribution of the device was similar to that under NIR light, the electron concentration in the TeSe shell was higher than the hole concentration, and the hole concentration in Te was higher than the electron concentration, indicating that there was an electric field from Te to TeSe that drove the migration of photogenerated carriers (Figures S10 and S11a, Supporting Information). Further, the results confirmed the mechanism by which the heterostructure Te@TeSe NWs had higher responsivity and photoconductive gain than pristine Te NWs.<sup>[27]</sup>

**Figure 4a** illustrates the  $I$ - $V$  curves of the photodetector illuminated by a 1550 nm laser with different optical power densities. The linear  $I$ - $V$  characteristic of the photodetector reveals the ohmic contact between the nanowire arrays and electrodes,

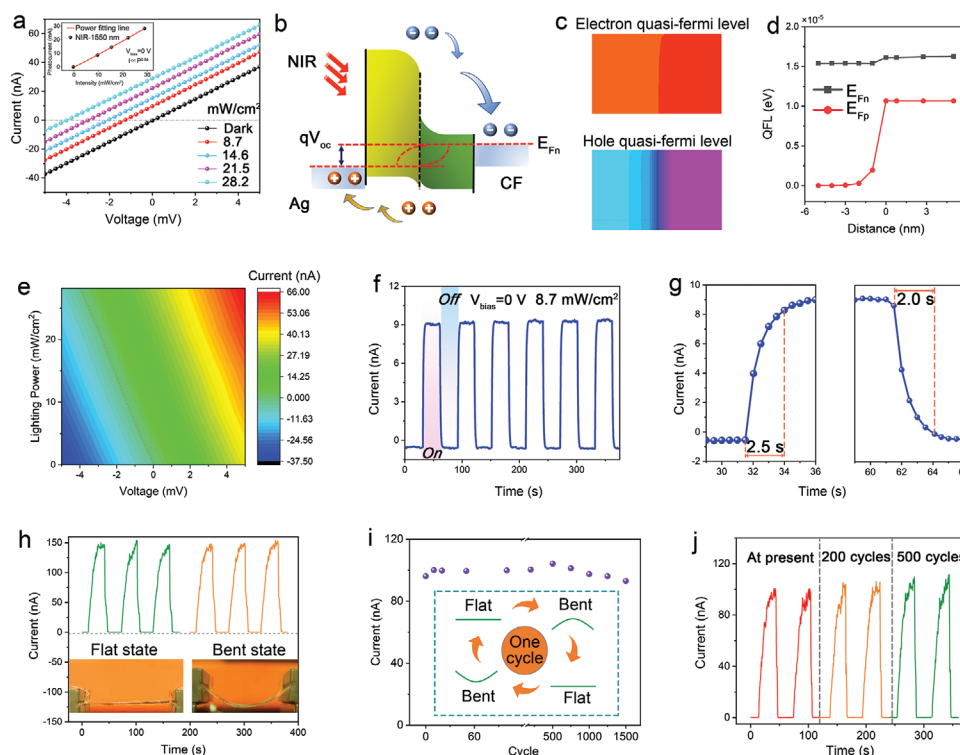


**Figure 4.** Te@TeSe nanowire arrays photoelectric property performance characterization. a)  $I$ - $V$  curves of the photodetector illuminated by 1550 nm laser with different optical power density. b) Energy band diagram of Te@TeSe nanowire arrays under NIR. c) Theoretical model of electron and hole quasi-Fermi level of Te@TeSe nanowire arrays under NIR. d) Quasi-Fermi level change according to FEM modeling Te@TeSe nanowire arrays under NIR. e) Colormap of photocurrent generation relating to the lighting power and bias voltage. f)  $I$ - $T$  curves of the photodetector under  $8.7 \text{ Mw cm}^{-2}$  1550 nm laser at 0 V bias voltage. g) The rise time and fall time of device. h) Time-dependent photoresponse curves under flat and bended. The inset is the images of the photodetector flat and bended. i) Bending cycle-dependent current curves. The inset is the schematic of one cycle. j) Time-dependent photoresponse curves under different bending angles at zero bias.

which is an important basis for the excellent performance of the photodetector. In addition, the slope of the  $I$ - $V$  curves is almost constant, suggesting that the internal resistance of the device remains almost constant, and the  $I$ - $V$  curves do not pass through the zero point, indicating that the device also has a photogenic volt effect, which can be used to fabricate self-powered photodetectors. The photogenic volt effect can be explained by the asymmetric structure of the Te@TeSe NWs. Along the nanowire direction, one end was Te, and the other end was TeSe. After Te contacted with TeSe, a type-II heterojunction band could be formed. In the absence of illumination, the heterostructure relied on the thermal motion of the electron hole to reach the thermal equilibrium state. There was a unified Fermi level in the heterostructure, and the valence and conduction bands were also in equilibrium (Figure S11b, Supporting Information). When the Te@TeSe NWs were illuminated, the photogenerated carriers in the depletion region were affected by the internal electric field, and the photogenerated electrons were transferred to Te, while the photogenerated holes were transferred to TeSe (Figure 4b). Therefore, electrons accumulated in Te and holes in the TeSe alloy, which resulted in a difference in the charge distribution between the two sides of the Te@TeSe NW, which was shown to be a potential difference. The modeling results (Figure 4c) show that under illumination, owing to the new electron hole pairs in the heterostructure,

the electrons and holes migrate to the opposite side to produce non-equilibrium carrier accumulation; consequently, the Fermi energy levels no longer coincide. That is, the potential is formed by the difference in space charge distribution. This conclusion was consistent with the theoretical results (Figure 4d). Thus, when the external circuit was connected to form a loop, the photodetector provided a corresponding potential output according to the light to complete the conversion of the optical signal to an electrical signal.

To verify the photoelectric response behavior of the Te@TeSe NW array photodetector, we measured the  $I$ - $V$  characteristic curves of the Te@TeSe NW array-based device under other near-infrared bands. The photodetector maintained a very stable signal output at 1064 and 1342 nm, and the photocurrent and light intensity showed a linear relationship (Figure S12, Supporting Information). Further, Figure 4e illustrates the relationship between the photocurrent, drain voltage, and light power, photocurrent mapping was visualized. The dotted line in Figure 4e indicates that the current value is zero, and the photoelectric voltage and applied bias in the circuit are of the same magnitude, but the signs are opposite. The curve is the relationship between the light intensity and the photoelectric potential. Moreover, the photocurrent's dependence on the optical power density was close to linear, which could be more intuitively observed through the  $I$ - $T$  curves of the photodetector

illuminated by 1550 nm with different optical power densities (Figure S13, Supporting Information). The relationship could be expressed as a power law,  $I = aP^b$ , where  $I$  is the photocurrent,  $a$  the constant,  $P$  the optical power intensity, and  $b$  an empirical value.<sup>[28]</sup> As can be seen, the experimental values were fitted and gave an exponential relationship of  $\approx I - P^{0.94}$ , indicating a near-linear dependence of photocurrent on the optical power intensity. Figure 4f shows that the  $I$ - $T$  curve of the Te@TeSe nanowire array photodetector maintains a consistent waveform over multiple cycles. It exhibited excellent stability and reversibility without obvious photocurrent decay. When the light was turned on, the current rapidly increased to a stable value, and when the light was turned off, it rapidly decreased to its original value. In Figure 4g, the rise time from 0% to 90% is  $\approx 2.5$  s and the fall time from 90% to 10% is  $\approx 2.0$  s. Indeed, the Te@TeSe nanowire array photodetectors were stable under periodic illumination and have the characteristics of short response time and self-power.

Nanowires are considered an important part of flexible electronic devices owing to their good mechanical ductility and flexibility.<sup>[29–32]</sup> The Te@TeSe nanowire array photodetector was based on flexible CFFs, which meant it has the intrinsic advantage of building flexible electronics.<sup>[33]</sup> The mechanical stability of nanowire-based photodetectors was studied to confirm their application prospects in flexible electronics. Considering the purpose of communication, collimating NIR with a wavelength of 1550 nm served as the light source. For communication purposes, the photodetector was attached to a piece of flexible polyethylene terephthalate via double-sided carbon tape to control the bending angle. The time-dependent photoresponse curves at a 0 V bias had a similar photocurrent and exhibited reproducible characteristics under periodic light illumination (Figure 4h). Figure 4h's inset shows the bent and flat states. Furthermore, the Te@TeSe nanowire array photodetector could not only be used under deflected conditions, but also showed excellent stability after dozens of bending. One cycle was defined as bending the device to a certain angle (see Figure 4i's inset), followed by reverse bending at the same angle, and finally turning to the original state. After bending the device for 200 and 500 cycles, the current rapidly decayed to the initial value when the light was turned off, indicating that it was stable and had a short response time (Figure 4j). Even after bending the device for 1500 cycles, the current remained around a certain value of 100 nA, indicating that the Te@TeSe nanowire array photodetector was very stable. From the flexible test, the device proved to have excellent stability and is promising for wearable electronics usage. In addition, Figure S14, Supporting Information, shows that the device based on a single fiber also has excellent stability, which means it can be woven into wearable devices through traditional weaving techniques.

## 2.4. Optical-Machine Communication Applications

In the experiments, the Te@TeSe nanowire array photodetector textiles responded well to near-infrared light with a wavelength of 1550 nm, which is a common communication band. This also means that the photodetector has potential for use in flexible and wearable devices in the field of optical communication.

Because it can be applied to an early warning system, when people enter a dangerous area, our device will sound an alarm by identifying the light signal to avoid injury. Among them, the sources of light signals can vary, including infrared radiation, special communication light waves, and linear lasers. Figure 5a shows the device's concept application in the early warning system: Te@TeSe nanowire arrays based on carbon fiber are woven into a fabric. When the external optical signal is received, a corresponding photoelectric potential is generated inside the device, which provides an electrical signal for subsequent reading circuits with a 0 V bias. This electrical signal is amplified by the corresponding circuit, and the contained information is conveyed and displayed. To demonstrate this conceptual application, a 1550 nm laser was used as the signal source, and the illumination of the laser was used as an analog signal. Figure 5b shows the switch status of the device woven on clothes. A voltage signal was obtained through the device, and the LED was controlled on and off after the amplification of subsequent circuits (Figure S15, Supporting Information).

Furthermore, the two states of the LED correspond to Morse code's dots and dashes or digital signals 0 and 1, which means that devices can be used to transmit more complex information. Figure 5c illustrates the application of the photodetector in optical-machine communication, that is, light controls the robotic manipulators to make certain gestures. There is an optical-machine communication flow chart: first, encode the microprocessor: read an electrical signal every second; the signal above the threshold is set to 1, otherwise, 0 (Figure 5d). Half of the maximum photoelectric voltage is taken as the threshold value to reduce signal reading time. The microprocessor reads four signals in a row, waits for a second, and displays a gesture corresponding to the light signal. Second, a set of signals is simulated with light, which the device accepts and converts into voltage signals. The electrical signal is amplified, de-noised, and transferred to the microprocessor. According to a preset password, the controller controls the robotic manipulators to perform the corresponding actions. When an NIR is encoded, the signal detected by the photodetector textile attached to the robotic manipulators is conditioned and converted into a switching signal for electrical appliances. Movie S1, Supporting Information, and Figure 5e show that the robotic manipulators were controlled by NIR to make some gestures: 1, 2, 3, and OK. Based on this system, many kinds of applications can be accomplished by simply rewriting the corresponding code into a single-chip microcomputer, which opens a new interactive method for optical mechanical communication.

## 3. Conclusion

Here, a self-powered, non-contact mechano-optical communication system based on a wearable Te@TeSe photodetector textile was demonstrated. As an NIR signal collector, the photodetector identifies external NIR commands and converts them into digital signals to modulate the robotic manipulators remotely, accurately, and quickly through an optical communicator. To benefit from the advantages of the type-II heterojunction of Te@TeSe NWs, the wearable photodetector textile has a higher photocurrent and responsivity, especially about 400 times



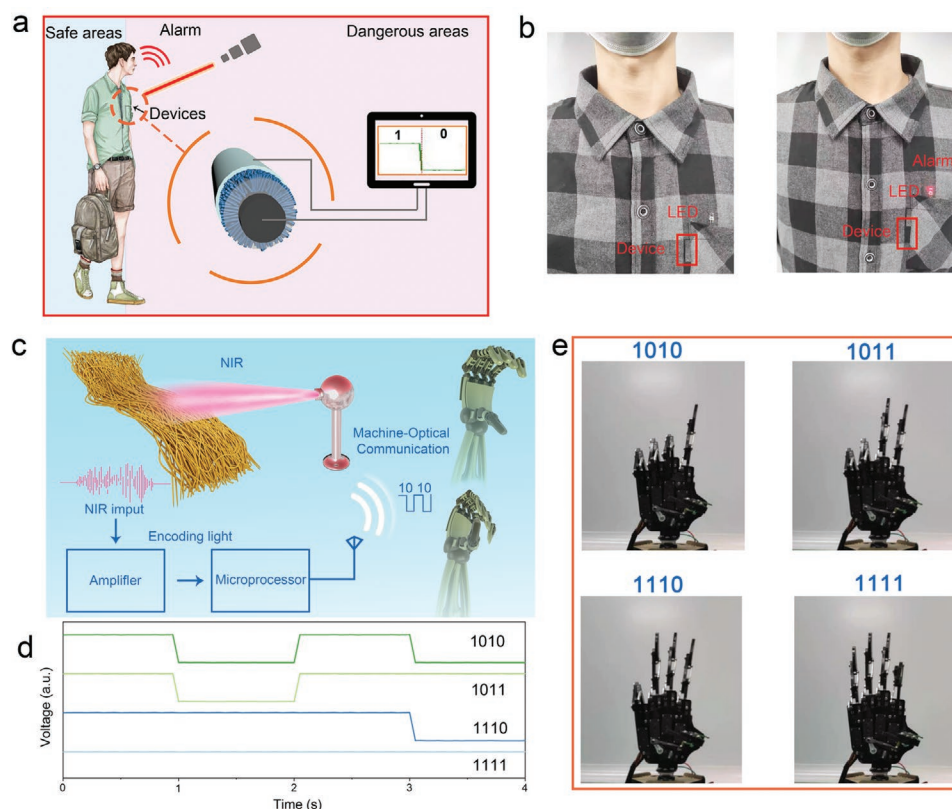


**Figure 5.** Optical-machine communication applications. a) Schematic and b) optical image of photodetector as warning system. c) Schematic illustration of optical-machine communication. d) The first signal is the encoded light signal of 1010, 1011, 1110, and 1111. e) Application of the photodetector as a communication device to modulate robotic manipulators actions.

at 1550 nm compared with pristine Te NWs, which was proven by first-principles calculations and simulated. Based on the mechano-optical communication system, we demonstrated an alarm control example and a basic optical-machine interactive application (robotic manipulator action, reach, and grasp of robotic manipulators). This system uses controlled lighting to achieve efficient signal conversion to drive a mechano-optical communication system and provide an innovative interface for IoT services.

## 4. Experimental Section

**Pretreatment of Carbon Fiber Fabric:** The CFF was soaked in hydrochloric (HCl) solution for two days. Then the CFF was placed in ethanol via ultrasonic cleaning to remove small particles of organic impurities. Finally, deionized water was used to wash away HCl.

**Synthesis of Te NW Arrays:** 50 mg Te as a raw material was placed in the center of quartz tube. Then, the CFF substrate was stuck on the downstream of the quartz tube, where temperature held low during growth. Before growth of the material, the air pressure in the tube was 20 Pa, and Argon gas flow was 50 sccm (standard cubic centimeters per minute). When the material began to grow, the PE source was opened to generate plasma, and the temperature in the tube furnace rose swiftly to 550 °C in 35 min and kept the temperature for 30 min. Then, the temperature in the tube furnace reduced to room temperature naturally and Te NWs were found deposited on the CFF.

**Synthesis of Te@TeSe NW Arrays:** The synthesis of Te@TeSe NW arrays was similar to that of Te NW arrays. The first step was the synthesis of

Te NW arrays on CFF (Te/CFF). The second step was similar to the first, except that 50 mg Te was replaced with 50 mg Se, and Te/CFF replaced the CFF was shifted out slightly.

**Photodetector Fabrication:** A layer of PMMA was evenly spin-coated on the CFF with NW arrays, by rotating 30 s at 1000 rpm (revolutions per minute). Then, a layer of Ag NWs was spin-coated as the top electron and drop a little silver as a pin. The bottom electron of the device was CFF.

**Simulations:** First-principles calculations were performed utilizing the Vienna Ab initio Simulation Package (VASP) based on the density functional theory (DFT).<sup>[34,35]</sup> The electron exchange-correlation functional was treated within the generalized gradient approximation (GGA) of Perdew–Burke–Ernzerhof (PBE) and the projected augmented wave (PAW). The energy convergence threshold was set to be  $10^{-8}$  eV. The kinetic energy cutoff of the plane wave and the k-point meshes of the Brillouin zone (BZ) are set to be 600 eV and  $19 \times 19 \times 19$  in both geometric optimizations and self-consistent calculations, respectively. For DOS calculations, a  $31 \times 31 \times 31$  k-grid mesh was adopted to ensure high accuracy. The Gaussian smearing method with a width of 0.05 eV was employed, and the spin-orbit coupling (SOC) effects and van der Waals corrections were included in the electronic structures calculations. Ultra-thin slabs of Te and TeSe were cleaved from the optimized crystals along the (1 0 0) crystalline direction with a thickness of 6 chiral chains, the vacuum slab of 20 Å thick was appended to the crystal slabs to ensure the convergence of the chemical potentials.

The device simulations were conducted with Silvaco Atlas (version 5.0.10.R) on Te@TeSe NW and pristine Te NW. Considering the material characterization, the simulated pristine Te NW has a diameter of 100 nm and length of 10 μm, and the Te@TeSe NW has the same geometry except 1 nm thick TeSe sheath. The specific material parameters used are displayed in Table S1, Supporting Information.<sup>[36–38]</sup> An anode and

cathode were put on two ends of the NW and the contacts were set as ohmic contacts. A simulated 1550 nm wavelength NIR light with an intensity of 10 mW cm<sup>-2</sup> was used as light source.

**Device Characterization and Measurement:** A probe station supporting a semiconductor characterization system (Keithley B1500A) was utilized to measure the characteristic of the photodetector. The IR illumination source was a power-adjustable light source capable of outputting homogeneous light. All tests were performed at room temperature.

**Material Characterization:** The morphology and lattice structure of the NWs were characterized by scanning electron microscopy (SEM, SU8020) and TEM equipped with an energy dispersive spectroscopy (EDS) analyzer (JEOL JEM-2010F). The Raman spectra were obtained by a laser Raman confocal microscope (Renishaw inVia-Reflex) with an excitation laser of 532 nm. The X-ray diffraction (XRD) data were collected by an X-ray powder diffractometer (Rigaku D/Max-2550,  $\lambda = 1.5418$  Å). All of the characterizations were processed at room temperature.

## Supporting Information

Supporting Information is available from the Wiley Online Library or from the author.

## Acknowledgements

The authors sincerely acknowledge financial support from the National Natural Science Foundation of China (NSFC Grant No. 61625404, 61888102), Foshan Innovative and Entrepreneurial Research Team Program (Grant No. 2018IT100031).

## Conflict of Interest

The authors declare no conflict of interest.

## Data Availability Statement

Research data are not shared.

## Keywords

mechano-optical communication systems, near-infrared light, self-powered photodetector, wearable photodetector

Received: May 19, 2021

Revised: June 9, 2021

Published online:

- [1] L. Lu, C. Jiang, G. Hu, J. Liu, B. Yang, *Adv. Mater.* **2021**, *33*, 2100218.
- [2] S. Wang, J. Xu, W. Wang, G.-J. N. Wang, R. Rastak, F. Molina-Lopez, J. W. Chung, S. Niu, V. R. Feig, J. Lopez, T. Lei, S.-K. Kwon, Y. Kim, A. M. Foudeh, A. Ehrlich, A. Gasperini, Y. Yun, B. Murmann, J. B.-H. Tok, Z. Bao, *Nature* **2018**, *555*, 83.
- [3] J. Huang, X. Yang, J. Yu, J. Han, C. Jia, M. Ding, J. Sun, X. Cao, Q. Sun, Z. Wang, *Nano Energy* **2020**, *69*, 104419.
- [4] Z. Wang, J. An, J. Nie, J. Luo, J. Shao, T. Jiang, B. Chen, W. Tang, Z. Wang, *Adv. Mater.* **2020**, *32*, 2001466.
- [5] M. Sitti, D. S. Wiersma, *Adv. Mater.* **2020**, *32*, 1906766.

- [6] S. Cai, X. Xu, W. Yang, J. Chen, X. Fang, *Adv. Mater.* **2019**, *31*, 1808138.
- [7] C. Bao, J. Yang, S. Bai, W. Xu, Z. Yan, Q. Xu, J. Liu, W. Zhang, F. Gao, *Adv. Mater.* **2018**, *30*, 1803422.
- [8] B. Fang, S. C. Bodepudi, F. Tian, X. Liu, D. Chang, S. Du, J. Lv, J. Zhong, H. Zhu, H. Hu, Y. Xu, Z. Xu, W. Gao, C. Gao, *Nat. Commun.* **2020**, *11*, 6368.
- [9] Z. Zhu, Y. Gu, S. Wang, Y. Zou, H. Zeng, *Adv. Electron. Mater.* **2017**, *3*, 1700281.
- [10] Q. He, Y. Wu, Z. Feng, C. Sun, W. Fan, Z. Zhou, K. Meng, E. Fan, J. Yang, *Nano Energy* **2019**, *59*, 689.
- [11] Z. Huang, Y. Hao, Y. Li, H. Hu, C. Wang, A. Nomoto, T. Pan, Y. Gu, Y. Chen, T. Zhang, W. Li, Y. Lei, N. Kim, C. Wang, L. Zhang, J. W. Ward, A. Maralani, X. Li, M. F. Durstock, A. Pisano, Y. Lin, S. Xu, *Nat. Electron.* **2018**, *1*, 473.
- [12] K. Sim, Z. Rao, Z. Zou, F. Ershad, J. Lei, A. Thukral, J. Chen, Q. Huang, J. Xiao, C. Yu, *Sci. Adv.* **2019**, *5*, eaav9653.
- [13] B. Mayers, Y. N. Xia, *J. Mater. Chem.* **2002**, *12*, 1875.
- [14] R. Martin, G. Lucovsky, K. Hellawell, *Phys. Rev. B* **1976**, *13*, 1383.
- [15] C. Tan, M. Amani, C. Zhao, M. Hettick, X. Song, D.-H. Lien, H. Li, M. Yeh, V. R. Shrestha, K. B. Crozier, M. C. Scott, A. Javey, *Adv. Mater.* **2020**, *32*, 2001329.
- [16] Y. Wang, G. Qiu, R. Wang, S. Huang, Q. Wang, Y. Liu, Y. Du, W. A. Goddard III, M. J. Kim, X. Xu, P. D. Ye, W. Wu, *Nat. Electron.* **2018**, *1*, 228.
- [17] M. Brodsky, J. Smith, Y. Yacoby, R. J. Gambino, *Phys. Status Solidi B* **1972**, *52*, 609.
- [18] R. Geick, E. F. Steigmeier, H. Auderset, *Phys. Status Solidi B* **1972**, *54*, 623.
- [19] J. D. Joannopoulos, M. Schluter, M. L. Cohen, *Phys. Rev. B* **1975**, *11*, 2186.
- [20] S. N. Yannopoulos, *J. Mater. Sci.: Mater. Electron.* **2020**, *31*, 7565.
- [21] Q. A. Vu, Y. S. Shin, Y. R. Kim, V. L. Nguyen, W. T. Kang, H. Kim, D. H. Luong, I. M. Lee, K. Lee, D.-S. Ko, J. Heo, S. Park, Y. H. Lee, W. J. Yu, *Nat. Commun.* **2016**, *7*, 12725.
- [22] W. Ran, L. Wang, S. Zhao, D. Wang, R. Yin, Z. Lou, G. Shen, *Adv. Mater.* **2020**, *32*, 1908419.
- [23] L. Li, L. Gu, Z. Lou, Z. Fan, G. Shen, *ACS Nano* **2017**, *11*, 4067.
- [24] A. Costas, C. Florica, N. Preda, A. Kuncser, I. Enculescu, *Sci. Rep.* **2020**, *10*, 18690.
- [25] M. Hussain, S. H. A. Jaffery, A. Ali, C. D. Nguyen, S. Aftab, M. Riaz, S. Abbas, S. Hussain, Y. Seo, J. Jung, *Sci. Rep.* **2021**, *11*, 3688.
- [26] Y.-H. Lin, W. Huang, P. Pattanasattayavong, J. Lim, R. Li, N. Sakai, J. Panidi, M. J. Hong, C. Ma, N. Wei, N. Wehbe, Z. Fei, M. Heeney, J. G. Labram, T. D. Anthopoulos, H. J. Snaith, *Nat. Commun.* **2019**, *10*, 4475.
- [27] J. Y. Wu, D. L. Huang, Y. J. Ye, J. Y. Wang, W. Huang, C. Li, S. Y. Chen, S. Y. Ke, *J. Semicond.* **2020**, *41*, 122402.
- [28] L. Gu, S. Poddar, Y. Lin, Z. Long, D. Zhang, Q. Zhang, L. Shu, X. Qiu, M. Kam, A. Javey, Z. Fan, *Nature* **2020**, *581*, 278.
- [29] Z. Lou, G. Shen, *Adv. Sci.* **2016**, *3*, 1500287.
- [30] D. Wang, L. Wang, G. Shen, *J. Semicond.* **2020**, *41*, 041605.
- [31] Q. Liu, S. Ramakrishna, Y.-Z. Long, *J. Semicond.* **2019**, *40*, 111603.
- [32] X. Fu, L. Wang, L. Zhao, Z. Yuan, Y. Zhang, D. Wang, D. Wang, J. Li, D. Li, V. Shulga, G. Shen, W. Han, *Adv. Funct. Mater.* **2021**, *31*, 2010533.
- [33] Y. P. Zhang, L. L. Wang, L. J. Zhao, K. Wang, Y. Q. Zheng, Z. Y. Yuan, D. Y. Wang, X. Y. Fu, G. Z. Shen, W. Han, *Adv. Mater.* **2021**, *33*, 2007890.
- [34] L. J. Zhao, K. Wang, W. Wei, L. L. Wang, W. Han, *InfoMat* **2019**, *1*, 407.
- [35] L. J. Zhao, L. L. Wang, Y. Q. Zheng, S. F. Zhao, W. Wei, D. W. Zhang, X. Y. Fu, K. Jiang, G. Z. Shen, W. Han, *Nano Energy* **2021**, *84*, 105921.
- [36] C. H. Champness, *Can. J. Phys.* **1976**, *54*, 967.
- [37] T. S. Moss, *Proc. Phys. Soc., London, Sect. B* **1952**, *65*, 62.
- [38] G. D. Van Dyke, *J. Opt. Soc. Am.* **1922**, *6*, 917.